150 Shades of Green: Using the Full Spectrum of Remote Sensing Reflectance to Elucidate Color Shifts in the Ocean

Ryan A. Vandermeulen* [a,b], Antonio Mannino[b], Susanne E. Craig[b,c], and P. Jeremy Werdell[b]

[a] Science Systems and Applications, Inc., Lanham, MD, 20706, U.S.A.

[b] NASA Goddard Space Flight Center, Greenbelt, MD, 20771, U.S.A.; Antonio.Mannino-1@nasa.gov, Jeremy.Werdell@nasa.gov

[c] University Space Research Association, Columbia, MD, 21046, U.S.A.; Susanne.E.Craig@nasa.gov

* Correspondence: Ryan.A.Vandermeulen@nasa.gov; Tel.: +1-301-286-8966

Abstract

This article proposes a simple and intuitive classification system by which to define full spectral remote sensing reflectance ($R_{rs}(\lambda)$) data with a quantitative output that enables a more manageable handling of spectral information for aquatic science applications. The weighted harmonic mean of the $R_{rs}(\lambda)$ wavelengths outputs an Apparent Visible Wavelength (in units of nanometers), representing a one-dimensional geophysical metric of color that is inherently correlated to spectral shape. This dimensionality reduction of spectral information combined with the output along a continuum of wavelength values offers a robust and user-friendly means to describe and analyze spectral $R_{rs}(\lambda)$ in terms of spatial and temporal trends and variability. The uncertainty in the algorithm's estimation of spectral shape is demonstrated on a global scale, in addition to the utility of the algorithm to discern spectral-spatial-temporal trends in the ocean, on a per-pixel basis for the entire 22 year continuous ocean color (SeaWiFS and MODIS-Aqua) time-series. This technique can be applied to datasets of varying multi- and hyper-spectral resolutions, providing continuity between heritage and future satellite sensors, and further enabling an effective means of elucidating similarities or differences in complex spectral signatures within the constraints of two dimensions. This straightforward means of conceptualizing multi-dimensional variability can help maximize the potential of the spectral information embedded in remote sensing data.

Keywords: Ocean Color; Spectral Classification; Spectral Shape; Optical Water Types; Remote Sensing Reflectance; MODIS; SeaWiFS; VIIRS; HICO; Spatial-Spectral-Temporal Variability

1. Introduction

Every parcel of ocean, lake, estuary or river water on Earth has the potential to exhibit a relatively unique optical 'fingerprint' in the ultraviolet to near-infrared spectral domain based on the presence, dynamic concentration, and widely varying size/shape/composition of phytoplankton, other suspended particulate matter, and chromophoric dissolved organic matter (CDOM) present at an observed time and location (Kirk 1994). The distinctive manner in which each of these water constituents contribute to the total spectral absorption ($a(\lambda)$, m^{-1}) and backscattering ($b_b(\lambda)$, m^{-1}) coefficients determines the bulk inherent optical properties of the water. These optical properties are collectively manifested through the shape and amplitude of the corresponding spectral remote sensing reflectance ($R_{rs}(\lambda)$, sr^{-1}), which quantitatively describes the color of the ocean (Kirk 1994). Ocean color science proceeds via the reverse (inverse) process, namely the estimation of in-water optical properties from a measurement of $R_{rs}(\lambda)$. Consequently, the fundamental measurement of ocean color through $R_{rs}(\lambda)$ enables the synoptic observation of spatial and temporal dynamics of biogeochemically significant processes in the upper ocean using information obtainable from space-based radiometers.

Current and heritage global ocean color satellite radiometers typically include(d) 5-10 visible wavelengths, but an era of hyperspectral radiometry is emergent. It is reasonable to presume that $R_{rs}(\lambda)$ spectra comprised of more information (e.g. more sampled wavelengths) lend more degrees of freedom, and thus more possibilities to unravel and quantify the unique bio-optical nature of that water parcel (Schaepman et al. 2009; Vandermeulen et al. 2017). However, with each added layer of spectral information, it becomes increasingly challenging to accurately characterize the relationships between multiple, simultaneous data dimensions (i.e. coincident analysis of the spectral, spatial, and temporal domains). One feasible approach to examine the variability of spectral information over time and space is to translate the layered elements of the spectral domain into a one-dimensional variable of interest, such as chlorophyll-a (O'Reilly and Werdell 2019), or a single, characterizing wavelength of a bio-optical property (Austin and Petzold 1981; Maritorena et al. 2002). Constraining multiple layers (wavelengths) of multi- or hyperspectral $R_{rs}(\lambda)$ to one dimension subsequently enables that information layer to be comprehensively analyzed in relation to its temporal and spatial variability. However, conventional approaches to derive geophysical parameters from ocean color data utilize only several (~1-4) wavelengths of all available $R_{rs}(\lambda)$ measured by a satellite instrument, discarding potentially useful information that makes the water optically distinct.

This issue can be partially addressed through the use of spectral classification techniques, whereby full spectral $R_{rs}(\lambda)$ data are mechanistically or empirically segregated into discrete classes according to the spectral shape of $R_{rs}(\lambda)$. The concept of spectral classification implicitly assumes that similar shapes of $R_{rs}(\lambda)$ are generated from waters with analogous optical (e.g. $a(\lambda)$ and $b_b(\lambda)$) characteristics (Vantrepotte et al. 2012), making it a potentially useful and complementary tool for use within bio-optical inversion algorithms (Lubac and Loisel 2007) or as a weighting factor for algorithm development (Moore et al. 2014). Using all of the spectral information ensures that any diagnostic signals present are considered, and subtle spatio-temporal trends from the integrated ocean color signal can be examined in relation to global or regional scale ecological change.

Multiple methods have been employed for the use of spectral classification of $R_{rs}(\lambda)$ in ocean and lake waters, classifying anywhere from 6 – 23 distinct water types across the globe. Various unsupervised hierarchical and non-hierarchical clustering techniques, such as fuzzy c-means classification (Eleveld et al. 2017; Moore et al. 2009; Moore et al. 2014) , agglomerative Ward's linkage (Lubac and Loisel 2007), iterative self-organizing data analysis technique (ISODATA) (Mélin and Vantrepotte 2015), varimax-rotated Principal Component Analysis (Avouris 2019), maximum wavelength classification (Ye et al. 2016), and k-means clustering (Prasad and Agarwal 2016; Wei et al. 2016) have proven effective in discriminating water types for various applications. However, these techniques require large *in situ* or simulated training datasets, and thus the estimation and representativeness of classification types is largely dependent on the characteristics of these same datasets, which may often be regionally specific. In addition to the development required to utilize these techniques, the results of the cluster and/or principal component analyses yield dimensionless classes, which require some a priori knowledge of the dataset for interpretation.

Perhaps one of the most intuitive and globally adaptable classification techniques to date comes from Wernand et al. (2013), which is based on translating observed $R_{rs}(\lambda)$ to chromaticity coordinates that define the water hue, which is then used to define 21 discrete color classes used in the historically ubiquitous Forel-Ule scale (Ule 1892). This approach of examining the water hue obtained from the weighted visible spectral response of the human eye has been applied over a wide variety of water types (van der Woerd and Wernand 2015, 2018), and used to distinguish phytoplankton functional types (Dierssen et al. 2006), and is useful in differentiating water masses that may otherwise look identical when only examining a limited number of wavelengths from optical instrumentation output (Jolliff et al. 2018). The water hue can also be expressed in terms of the "dominant wavelength" of a given spectrum (Lehmann et al. 2018), providing an instinctual metric by which to classify optical water types, and is most closely aligned (though mechanistically distinct) to the approach we present in this manuscript. A limitation of being constrained by the spectral response function of the human eye (peak detection at 450 nm, 550 nm, and 600 nm, with minima at 400 nm, 500 nm, and 700 nm; (CIE 1932)), however, is inherently precluding the incorporation of ultraviolet (UV) and near-infrared (NIR) portions of the spectrum, which can encompass an important portion of biogeochemical variability (Pitarch et al. 2019). Regardless of methodology utilized, the value in exploiting full spectral information has been demonstrated repeatedly, and is imperative to maximize the utility of a new era of hyperspectral measurements from space (Hestir et al. 2015).

Here, we present a dynamic spectral classification index to quantitatively describe the shape of any multi- or hyperspectral dataset along a continuum of wavelength values to facilitate the conceptualization of simultaneous spectral-spatial-temporal variability in ocean color. The proposed technique can be applied indiscriminately to various water types, can be extended beyond the visible wavelengths (e.g. ultraviolet and near-infrared), does not require a training dataset or data transformation, is computationally cost-effective, and perhaps most importantly, produces a mappable output that is simple and intuitive enough to be interpreted and utilized by seasoned scientists, laypersons, and end-users alike. The functionality to simultaneously conceptualize multiple layers of information can not only help reveal ecologically significant trends, but also aid in the first-order utilization and interpretation of remotely sensed, high spectral resolution datasets, such as that obtained from airborne campaigns or the future slated National Aeronautics and Space Administration's (NASA) Plankton, Aerosol, Cloud, ocean Ecosystem (PACE) satellite mission (Werdell et al. 2019).

2. Materials and Methods

The proposed approach to spectral classification was applied to synthetically derived radiometric data, as well as satellite based radiometric data from the NASA Sea-viewing Wide Field-of-view Sensor (SeaWiFS) onboard Orb-View2, the Moderate Resolution Imaging Spectroradiometer onboard Aqua (MODIS-Aqua), the Visible Infrared Imaging Radiometer Suite (VIIRS) onboard Suomi-NPP, and the Hyperspectral Imager for the Coastal Ocean (HICO) onboard the International Space Station. These data are used to demonstrate various facets of the functionality and uncertainty of the proposed algorithm, as well as trends in the spectral-spatial-temporal variability of optical water masses. The datasets are described first, followed by a description of the classification approach, and various statistical approaches to assess uncertainty and trends.

2.1 Satellite Data

Level-3 monthly mean global binned images from SeaWiFS (September 1997 – December 2007; 9 km resolution), MODIS-Aqua (Jan 2003 – Dec 2019; 4 km resolution), and VIIRS (Jan 2012 – Dec 2019; 9 km resolution) were acquired from the NASA Ocean Biology Processing Group (OBPG; https://oceancolor.gsfc.nasa.gov/l3). An individual MODIS-Aqua rolling 32-day composite image (14 Sep – 15 Oct 2018) was also acquired. All visible $R_{rs}(\lambda)$ (SeaWiFS λ = 412, 443, 490, 510, 555, 670 nm , MODIS λ = 412, 443, 469, 488, 531, 547, 555, 645, 667, 678 nm, VIIRS λ = 410, 443, 486, 551, 671 nm) were retained. Satellite data processing followed the OBPG's R2018.0 reprocessing configuration (https://oceancolor.gsfc.nasa.gov/reprocessing/), which corrects for suspect late-mission global trends in the blue-band water leaving reflectance (Lee et al. 2019). The rolling 32-day composite $R_{rs}(\lambda)$ data were also processed to obtain the *hue angle* product (van der Woerd and Wernand 2015; van der Woerd et al. 2016), using the European Space Agency's Sentinel

Application Platform (SNAP) toolbox (https://step.esa.int). Additional regionally binned time-series data frequently used to test sensor stability from SeaWiFS, MODIS-Aqua, and VIIRS were obtained for a north Pacific region (20.0°N - 30.0°N, 179.0°W - 140.0°W) from the OBPG (https://oceancolor.gsfc.nasa.gov/docs/methods/sensor_analysis_methods/).

Level-2 HICO and MODIS-Aqua data were also obtained from the OBPG; (https://oceancolor.gsfc.nasa.gov/l2). HICO data were subsequently binned and mapped using the l2bin and l3mapgen software tools packaged as part of the NASA SeaWiFS Data Analysis System (SeaDAS; https://seadas.gsfc.nasa.gov), in order to match the nominal spatial resolution of a Level-2 MODIS-Aqua image (1-km), enabling a direct comparison. All visible $R_{rs}(\lambda)$ from HICO (λ = 404 - 696 nm, 5-6 nm resolution) were retained for subsequent analysis.

2.2 Synthetic Hyperspectral Data

A high spectral frequency dataset was acquired, comprised of 720 hyperspectral (5 nm resolution; 350 – 800 nm) synthetic observations of $R_{rs}(\lambda)$, $a(\lambda)$, $b_b(\lambda)$, phytoplankton absorption ($a_{ph}(\lambda)$; m^{-1}), detrital matter absorption ($a_d(\lambda)$; m^{-1}), CDOM absorption ($a_g(\lambda)$; m^{-1}), phytoplankton backscatter ($b_{b\text{-}ph}(\lambda)$; m^{-1}), and detrital matter backscatter ($b_{b\text{-}dm}(\lambda)$; m^{-1}). This synthetic dataset was created to provide a measurement error-free hyperspectral dataset as part of research performed by the first NASA PACE Science Team (NNH13ZDA001N-PACEST). To generate the above listed parameters, a synthetic dataset of sea surface and top of atmosphere (TOA) radiances were constructed by the Coupled Ocean Atmosphere Radiative Transfer (COART) model (Du and Lee 2014) based on the SBDART (Santa Barbara DISORT Atmospheric Radiative Transfer) code (Ricchiazzi et al. 1998), with the ocean contribution simulated by Hydrolight (Mobley and Sundman 2008). Water-leaving radiance (L_w) was forward modeled with Hydrolight, parameterized with a solar zenith angle of 30°, cloudless sky, a sea surface state corresponding to a wind speed of 5 $m\text{-}s^{-1}$, and realistic concentrations of optically active water constituents. The Hydrolight component of the model was constrained using inherent optical properties (IOPs) whose dynamic ranges and spectral qualities were based on *in situ* data acquired from the NASA SeaWiFS Bio-optical Archive and Storage System (SeaBASS) dataset (https://seabass.gsfc.nasa.gov/). Certain characteristics of the IOPs were semi-randomly modeled based on principles outlined in IOCCG Report No.5 (2006) and summarized in the accompanying PDF document provided along with this dataset. Atmospheric conditions were simulated by coupling the water-leaving radiances to an atmosphere with and without absorbing gases, and with an aerosol optical depth (AOD) that varied between 0.1-0.8. Note, while this synthetic dataset may not be inclusive of all possible combinations of R_{rs}/IOP variation found in the ocean, the models used to generate the dataset have been parameterized with a wide range of field-based measurements, and thus this dataset should be representative of a wide variety of realistic optical variations found in natural waters. Data and associated documentation can be found online at https://doi.pangaea.de/10.1594/PANGAEA.915747 (Craig et al. 2020).

2.3 Spectral Classification Technique

We describe the color of the water, and hence group spectral data, using a weighted harmonic mean of $R_{rs}(\lambda)$ wavelengths, constrained by the relative intensity of reflectance, outputting the 'Apparent Visible Wavelength' (hereafter *AVW*), in units of nanometers:

$$AVW = \frac{\sum_{i=\lambda_1}^{\lambda_n} R_{rs}(\lambda_i)}{\sum_{i=\lambda_1}^{\lambda_n} \frac{R_{rs}(\lambda_i)}{\lambda_i}} = \left(\frac{\sum_{i=\lambda_1}^{\lambda_n} \lambda_i^{-1} R_{rs}(\lambda_i)}{\sum_{i=\lambda_1}^{\lambda_n} R_{rs}(\lambda_i)} \right)^{-1} \qquad (1)$$

The weighted harmonic mean, as opposed to a weighted arithmetic mean, is utilized to enable equal weighting of the wavelengths in the calculation. If the *AVW* is derived from the weighted *arithmetic* mean, data points on the red (higher λ) end of the spectrum are automatically assigned more weight than points on the blue (lower λ) end of the spectrum. Using the weighted *harmonic* mean ensures the weights assigned are solely a function of R_{rs} intensity, and not the relative position within the visible electromagnetic spectrum. The derivation of the *AVW*, at its most fundamental level, is simply a first-order measure of the dominant color of the water, as determined by the weight that each measured reflectance channel contributes to the albedo in the visible (or UV/NIR, if incorporated) range of the spectrum. The output is not in the form of discrete classes, but instead a continuous gradient of wavelength values that represent a quantitative descriptor of weighted mean color reflected from the water's surface. At any point on this gradient, we find comparable $R_{rs}(\lambda)$ spectra represented by the same *AVW* number. Consider, for example, a discrete cluster of $R_{rs}(\lambda)$ spectra acquired from a global MODIS-Aqua 32-day composite (14 Sep – 15 Oct 2018), where *AVW* values fall between 510.00 – 510.99 nm (Figure 1). The global mean spectrum of this cluster, $R_{rs}(\lambda)'_{AVW=510nm}$ (Figure 1, black line), and 100 randomly selected normalized spectra with the same *AVW* value, $R_{rs}(\lambda)_{AVW=510nm}$ (Figure 1, gray lines), are shown to illustrate the distribution of spectral shapes represented by *AVW* = 510 nm.

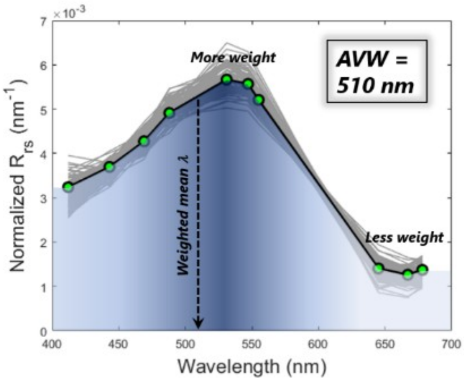

Figure 1. 100 random spectra defined by 510 ≤ *AVW* ≤ 510.99 nm extracted from a global MODIS-Aqua 32-day global composite (14 Sep – 15 Oct 2018) are plotted as gray lines, while the thicker black line represents the

global mean of all spectra within the 510 nm *AVW* cluster. Note, in order to reduce the first order (amplitude) variability and emphasize variations in spectral shape alone, the spectral $R_{rs}(\lambda)$ values in each cluster have been normalized to the trapezoidal integration of $R_{rs}(\lambda)$. An animation of this figure stepping in 1.0 nm increments between 505 – 515 nm further illustrates the sensitivity of *AVW* to characterize changes in the spectral shape of $R_{rs}(\lambda)$ (https://pace.oceansciences.org/rse.gif).

While the concept is admittedly simplistic in nature, it is surprisingly effective as an index of spectral shape. The location of the *AVW* effectively represents the balance point around which reflectance data is evenly distributed, or more informally, where a $R_{rs}(\lambda)$ spectrum would be perfectly balanced on the tip of a pin if each individual channel held a physical weight proportional to its intensity. If any slight weight is added on either side of the spectrum (e.g. a shift in color due to absorption or backscatter contribution), the balance point (*AVW*) will shift, unless it is offset by a proportional counter-balanced weight elsewhere in the spectrum. In this context, similar $R_{rs}(\lambda)$ spectral shapes tend to converge along the *AVW* gradient (Figure 2a), ultimately constrained by the finite number of combinations of absorption and backscattering (Figure 2b-2h) that create a particular $R_{rs}(\lambda)$ spectrum with an identical balance point. While the *AVW* serves here as an effective means of conveying information about spectral shape, it is important to note that this does not afford information on the absolute magnitude of a given spectrum (thought the two can often be closely correlated). The implications of this are further considered in Section 4.1.

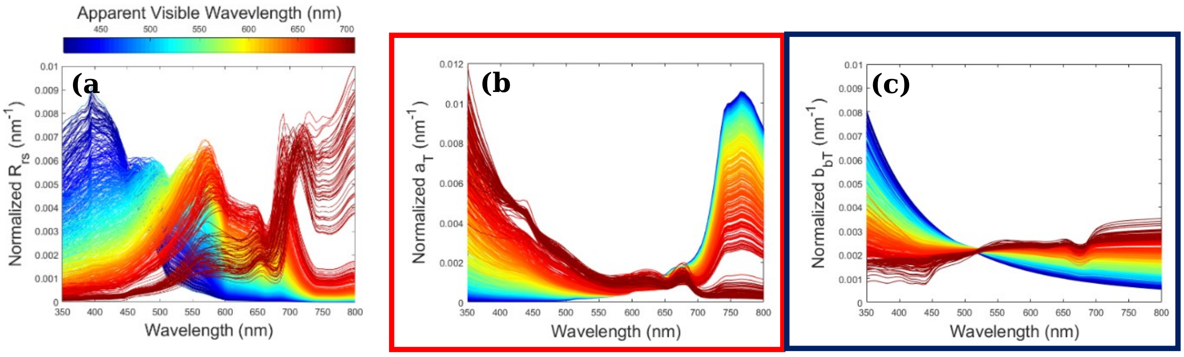

Absorption components
(phytoplankton, detrital matter,
CDOM)

Backscatter components
(phytoplankton, detrital
matter)

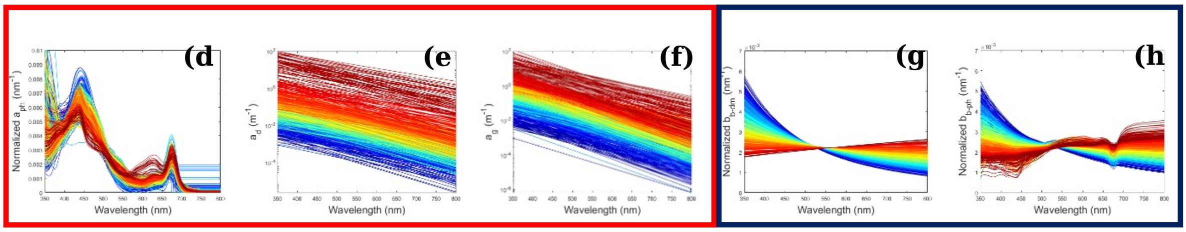

Figure 2. (**a**) *AVW* values were derived from the 720 synthetic $R_{rs}(\lambda)$ spectra, yielding a range of values from 412 – 708 nm. Changes in spectral shape of $R_{rs}(\lambda)$ from blue, oligotrophic waters to brown/green coastal waters follow the gradient of *AVW* values, which represents a gradual change in the central balancing point of the spectrum. (**b-h**). The corresponding inherent optical properties (total absorption, total backscatter, and their respective sub-contribution from phytoplankton, CDOM, and detrital matter) contribute directly to the $R_{rs}(\lambda)$ signal, and also follow a unidirectional gradient of *AVW* values.

2.4 How well does the AVW describe spectral shape?

Since we are relying on the *AVW* as an index of $R_{rs}(\lambda)$ spectral shape, it is useful to define a measure of whether the spectra categorized by *AVW* are the same or significantly different from one another. For this manuscript, we will characterize these differences for a global MODIS-Aqua 32-day composite (14 Sep – 15 Oct 2018) to serve as an example of the relative effectiveness with which the *AVW* can categorically define $R_{rs}(\lambda)$ by its spectral shape. Assuming a narrow range of *AVW* can be used to define a distinct group of $R_{rs}(\lambda)$ that share similar spectral characteristics (e.g. Figure 1), we can proceed by quantifying the Type A uncertainty for each MODIS-Aqua wavelength ($u_a(\lambda)$, ISO and OIML (1995)); as a function of *AVW*:

$$u_a\left(\lambda, AVW\right)=\sqrt{\frac{\sum_{i=1}^{n}\left(R_{rs}\left(\lambda, AVW\right)_i - R_{rs}\left(\lambda,{}^{\prime}AVW\right)\right)^2}{\left(n-1\right)}}$$

(2)

where n = the total number of $R_{rs}(\lambda)$ spectra that fall within each 1 nm increment of *AVW*. Note, for statistical analysis of global MODIS-Aqua imagery, we only defined the uncertainty if the *AVW* defined at least 250 spectra. This threshold was implemented as a quality control measure to mitigate the inclusion of erratic spectral shapes due to errors in satellite data processing or ocean color atmospheric correction. This resulted in the exclusion of only 0.01% of the 16,633,461 total global spectra from the analysis.

2.5. Obtaining continuity across various spectral platforms

Datasets containing disparate band-placement (e.g. hyperspectral versus SeaWiFS versus MODIS-Aqua versus VIIRS) will unequivocally yield a discontinuity in *AVW* values. These differences are to be expected given the inherent variations in absolute spectral shape output from different satellite sensors and they demonstrate the sensitivity of *AVW* to subtle changes in spectral shape, even if they are a result of spectral band placement. To correct for this, we use a similar approach to van der Woerd and Wernand (2015), by which a synthetic hyperspectral dataset is utilized to produce sensor specific polynomials. First, $R_{rs}(\lambda)$ for each multispectral sensor are reconstructed from the 720 hyperspectral synthetic spectra, using the corresponding Relative Spectral Response (RSR) function for each satellite sensor, acquired from the OBPG (https://oceancolor.gsfc.nasa.gov/docs/rsr/rsr_tables/). The hyperspectral *AVW* is calculated from the truncated hyperspectral synthetic data (Figure 3a, with only 400 – 700 nm used in the calculation for compatibility with the visible range of Level-3 products distributed with heritage sensors), and compared to the multispectral *AVW* calculated for each sensor, and the coefficients from a 3rd or 4th order polynomial fit are retained and applied to satellite data (Table 1, Figure 3b). We demonstrate the correction on a regional north Pacific time series processed by the OBPG, which includes SeaWiFS, MODIS-Aqua, and VIIRS, showing the initial offset of *AVW* values (Figure 3c), followed by the convergence of *AVW* after the correction is applied (Figure 3d).

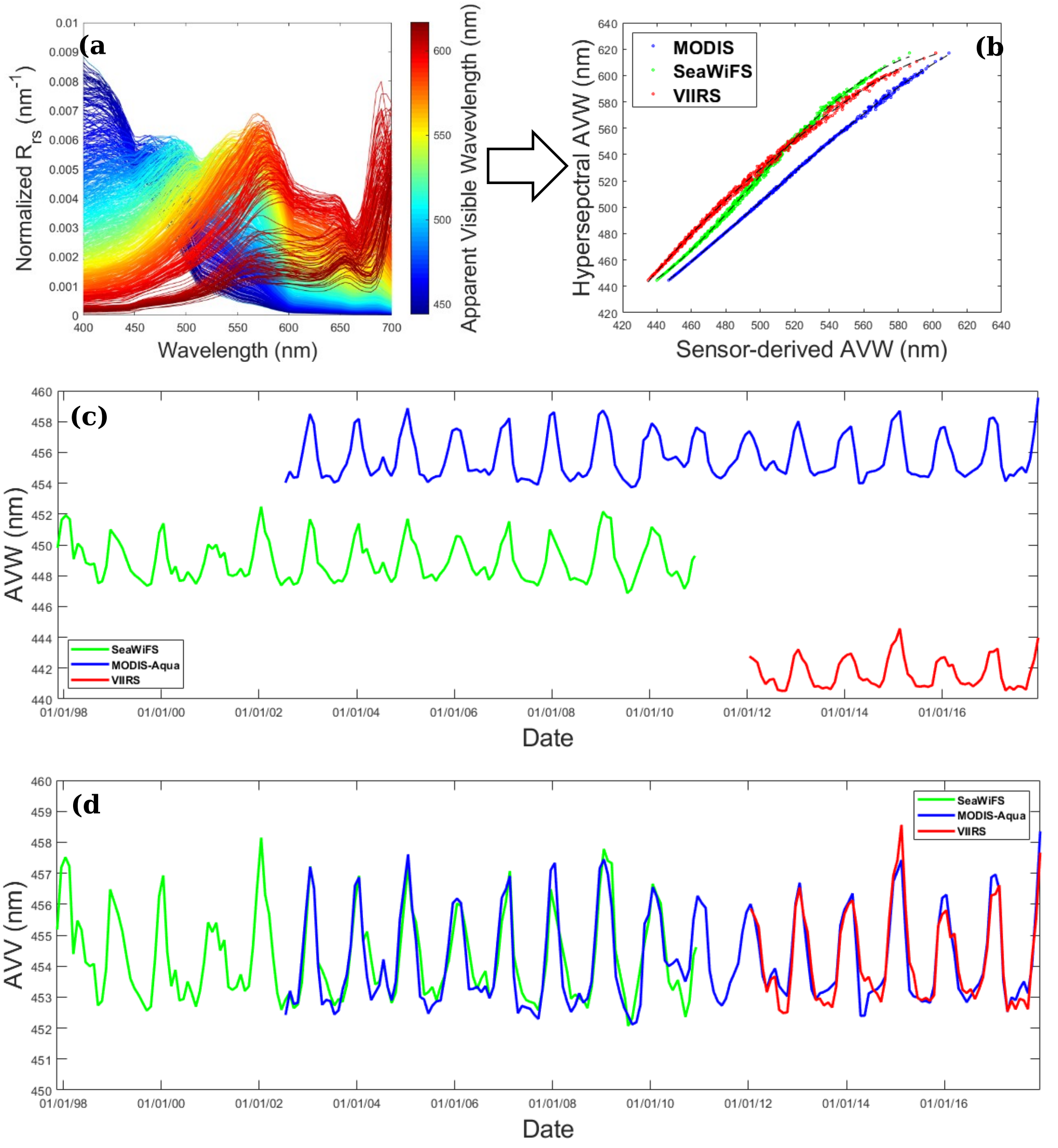

Figure 3. (**a**) The *AVW* applied to a spectral subset (400 – 700 nm) of the hyperspectral synthetic $R_{rs}(\lambda)$ dataset was used as the basis to form (**b**) sensor specific conversion coefficients for MODIS-Aqua, SeaWiFS, and VIIRS. A cross-mission regional time-series in the north Pacific Ocean was used for temporal trend analysis, showing (**c**) the discontinuity in *AVW* values without correction, and (**d**) the subsequent convergence of *AVW* values after the coefficients are applied.

Table 1. Polynomial coefficients to calculate a hyperspectral-equivalent *AVW* are listed for MODIS-Aqua, SeaWiFS, and VIIRS. Though not included in our analysis, given the significance of the Sentinel-3 platforms for continuity in the ocean color time-series, we also include coefficients for the Ocean and Land Colour Instrument (OLCI). Note, for compatibility with the distribution of Level 3 $R_{rs}(\lambda)$ products distributed through OBPG (which are limited to the visible range of the spectrum), the OLCI coefficients do not include contribution from the 709 nm band.

Sensor	**Polynomial Coefficients**				**Intercept**
	x^4	**x^3**	**x^2**	**x**	
MODIS	N/A	-1.19797×10^{-5}	1.81042×10^{-2}	-7.96725	1.45896×10^{3}
SeaWiFS	1.83929×10^{-7}	-4.22090×10^{-4}	3.55860×10^{-1}	-1.29806×10^{2}	1.77270×10^{4}
VIIRS	-1.22955×10^{-7}	2.50561×10^{-4}	-1.93331×10^{-1}	6.80274×10^{1}	-8.78677×10^{3}
OLCI	-1.55476×10^{-8}	4.16732×10^{-5}	-4.04673×10^{-2}	1.77929×10^{1}	-2.50184×10^{3}

2.6. Assessing the utility of AVW across various spectral platforms

The linear trends later presented in this manuscript are derived from multiple satellite platforms, therefore it is prudent to assess the "fitness-for-purpose" of the individual mission contribution to the combined time-series. One way to examine this is by comparing shorter-term trend patterns from overlapping temporal periods within the satellite data record, to ensure that there is no substantial disagreement between disparate sensors (Mélin et al. 2017). In this manuscript, we examine separate periods of overlapping *AVW* data for SeaWiFS and MODIS-Aqua (Jan 2002 – Dec 2006; representing a period of optimal sensor performance and no data gaps from SeaWIFS) and MODIS-Aqua and VIIRS (Jan 2012 – Dec 2017; representing the inclusion of reprocessed, well-characterized R2018.0 MODIS-Aqua data from the OBPG; Lee et al. (2019)). Following the methodology of Mélin et al. (2017), we generated a contingency matrix (Sokal and Rohlf 1995) to compare trend diagnostics, which defines what percent of the globe demonstrates agreement/disagreement in the directionality of slope, β. The Cohen's κ index (Viera and Garrett 2005) can be computed from this table, describing the level of agreement (poor/moderate/substantial) in the directionality of β derived from two sensor overlap periods. Finally, to more quantitatively assess the differences in the absolute magnitude of β, we examined the level of significance (p) of a t-test comparing trends derived from two overlapping missions. In this context, a lower p-value would equate to a significant difference in trends. Thus, we can determine what percent of the globe exhibits significantly different trends ($p < 0.05$) when comparing two missions (Mélin et al. 2017).

2.7 Time Series Trends

Temporal linear trends across 22-years of seasonally detrended *AVW* values from SeaWiFS (Sep 1997 – Dec 2002), MODIS-Aqua (Jan 2003 – Dec 2019) are determined using an iteratively reweighted least squares robust regression with a bisquare weighting function that mitigates the biasing influence of outlier values (see robustfit MATLAB function (Dumouchel and O'Brien 1992; Holland and Welsch 1977). Prior to determining the linear trends, the annual cycle of *AVW* was determined as the monthly averages of the combined time-series, and the data were de-seasonalized by subtracting the contribution of the corresponding monthly climatology, thereby reducing the impacts of autocorrelation associated with strong seasonality. The derived slope (β) from the robust regression (only performed if at least 3 months of data per year are present) is used to determine ***Δ****AVW/****Δ****time*, which is interpreted as a metric of directional shift in spectral shape as a function of time. A positive β, for example, indicates a red shift (that is, a stronger contribution from longer wavelengths). All β terms with non-significant probability values ($p > 0.05$; derived from the robustfit stats function) are excluded from the generated maps, and the standard error (*se*, derived from MATLAB robustfit function) of the regression is retained as an additional quality metric.

3. Results

3.1. Examining global R_{rs} variability

The *AVW* algorithm was applied to a rolling 32-day composite global image retrieved from MODIS-Aqua (Figure 4a), and the corresponding $R_{rs}(\acute{\lambda})_{AVW}$ were identified for each 1 nm increment of *AVW* (Figure 4b). The distribution of *AVW* values range along a gradient from 448 nm (very oligotrophic waters with a strong signal in the blue end of the spectrum) to 575 nm (very turbid waters with a strong signal in the red end of the spectrum). Regional extractions (Figure 4c-4e) are shown to emphasize the detail in the gradational change of the *AVW* index.

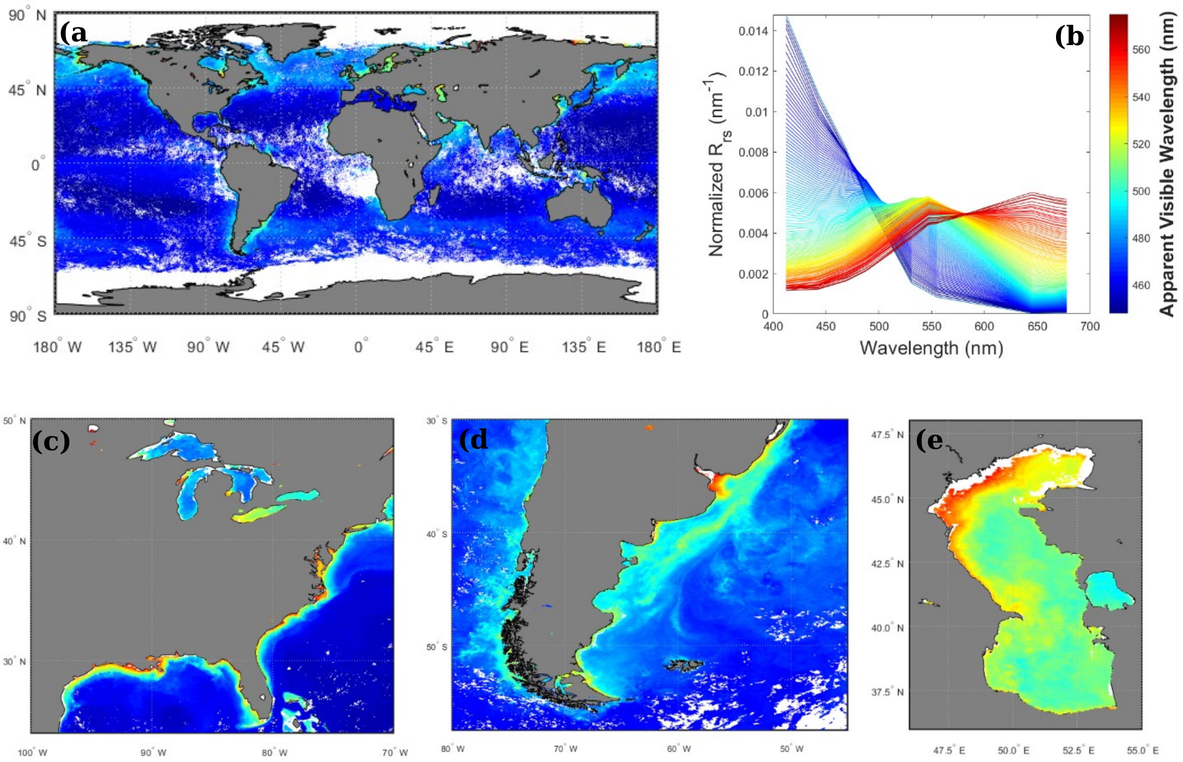

Figure 4. (**a**) Global map of *AVW* for a 32-day global composite (14 Sep – 15 Oct 2018). (**b**) Integral-normalized $R_{rs}(\lambda)$ spectra, corresponding to the 1 nm *AVW* clusters defined for the global composite. Zoomed regions of interest show details of the *AVW* gradients along the (**c**) U.S. East Coast, Great Lakes, and northern Gulf of Mexico, (**d**) southern South America, and (**e**) the Caspian Sea.

Given the nature of the gradational output, spectral shape uncertainty is best determined for each individual MODIS-Aqua channel across the range of *AVW* values, in order to quantify how well normalized $R_{rs}(\lambda)_{AVW}$ are represented by the corresponding $R_{rs}(\acute{\lambda})_{AVW}$ (i.e. how representative is Figure 4b in characterizing the global distribution of spectral shapes?). Below, we report variance (in terms of Type 1 uncertainty and % coefficient of variation, % CV) of $R_{rs}(\lambda)_{AVW}$ for each MODIS-Aqua channel, in relation to its respective $R_{rs}(\acute{\lambda})_{AVW}$ spectra. We found the analysis more informative than, for example, spectral similarity indices, as the chosen metrics describe the spectral dependence of shape deviations. Figures 5a shows that Type 1 uncertainty is generally highest for the 412 nm channel, shifting to higher uncertainty in 547 nm and 555 nm channels in more turbid waters. All channels exhibit the highest amount of collective uncertainty in the adherence to a defined spectral shape in predominately green waters, characterized as *AVW* > 500 nm. On average, the uncertainty at each channel is <5% for blue waters (AVW<480 nm), and <10% for green/red-shifted waters. Note, the high % CV for far red and far blue channels are representative of much lower average values in reflectance (Figure 4b). The origin of the overall uncertainty and its implications are discussed further in section 4.1.

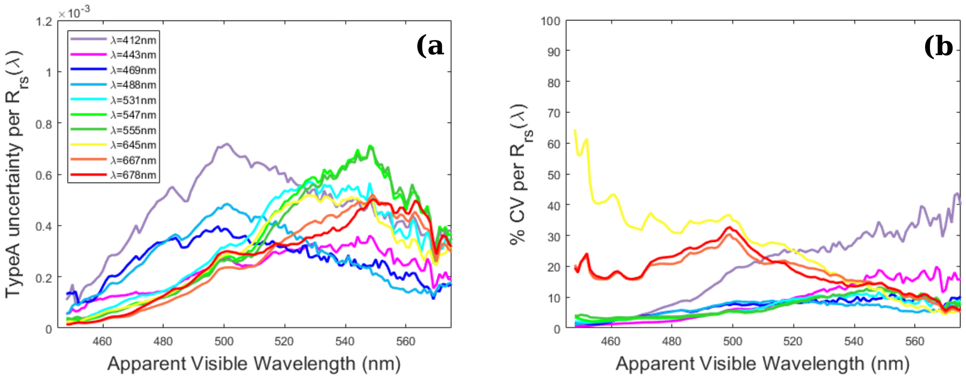

Figure 5. For each MODIS-Aqua wavelength, we quantify the (**a**) Type 1 uncertainty and (**b**) % CV as a function of 1 nm incremental $R_{rs}(\acute{\lambda})_{AVW}$ spectra derived from the MODIS-Aqua 32-day global composite (14Sep – 15Oct 2018).

3.2. *Examining R_{rs} trends in the spatial domain*

Since the coefficients used to derive cross-sensor (hyperspectral equivalent) *AVW* are computed from an ideal synthetic dataset, it is a useful exercise to validate these coefficients against a less ideal dataset that likely contains spectral shapes from which the coefficients have not been trained. Thus, as an initial test on the spatial integrity of the *AVW*, we sought to test the algorithm on HICO imagery, representing an independent spatially resolved hyperspectral dataset with real satellite-based uncertainties resulting from calibration errors, atmospheric correction, land/cloud adjacency effects, and potential bottom reflectance effects that can impact the spectral shape of $R_{rs}(\lambda)$ *(Ibrahim et al. 2018)*. First, we spatially co-registered a HICO (52 visible bands) and MODIS-Aqua (10 bands) image to 1 km spatial resolution in order to enable direct comparisons. To initiate the check on the sensors' derived polynomials, we constructed a 'false' MODIS image, in which HICO data (interpolated to 1 nm spectral resolution) were spectrally subsampled to MODIS wavelengths (using the RSR of MODIS-Aqua). The polynomials derived from the synthetic dataset were applied to the constructed MODIS-Aqua image to create a hyperspectral equivalent *AVW* from MODIS-Aqua bands, and then directly compared to the *AVW* values derived from the HICO image (Figure 6). This first check essentially tells us how well the idealized synthetic dataset represents the range of data found in the HICO image. Figure 6 shows a close relationship ($r^2 = 0.9995$) between the HICO data and the constructed MODIS-Aqua data, lending confidence that a cross-comparison of *AVW* values derived from MODIS-Aqua and HICO would be meaningful.

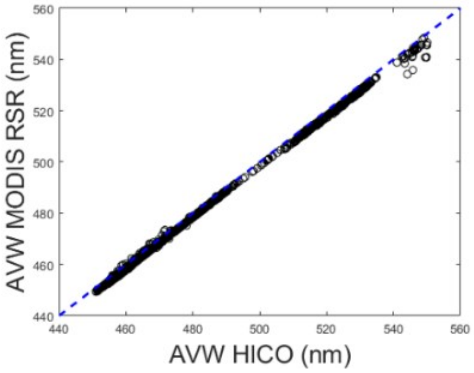

Figure 6. A comparison of 3,094 coincident *AVW* values derived from HICO and a 'false' MODIS-Aqua image constructed from HICO data. This comparison serves as validation for the sensor-specific polynomials derived from the synthetic dataset applied to MODIS-Aqua data.

We next proceed with calculating the polynomial-corrected *AVW* for the actual coincident MODIS-Aqua and HICO images (Figure 7a, 7b), then examine the difference of the two images (Figure 7c). Given the spatial integrity of the *AVW* algorithm demonstrated across the two spectral resolutions (Figure 6), and minimal temporal disconnect (note, the two images are temporally disconnected by only 16 minutes in overpass time), the differences seen in the two images should solely be a function of absolute differences in spectral shape as detected from the disparate sensors. The extracted spectra from three points of interest corroborate the patterns shown in the difference image, e.g. where $AVW_{HICO} > AVW_{MODIS}$ (Figure 7d), the HICO spectra is red-shifted relative to MODIS-Aqua, where $AVW_{HICO} < AVW_{MODIS}$ (Figure 7f), the HICO spectra is blue-shifted relative to MODIS-Aqua, and where $AVW_{HICO} = AVW_{MODIS}$ (Figure 7e), the HICO and MODIS-Aqua spectral matchup is nearly equivalent. Regardless of what mechanisms cause the differences between the two images (e.g. contrasting SNRs or potential atmospheric correction errors), the dimensional reduction of spectral information through *AVW* enables the functional examination of the directionality and magnitude of the sensor disparities within the constraints of a two dimensional image.

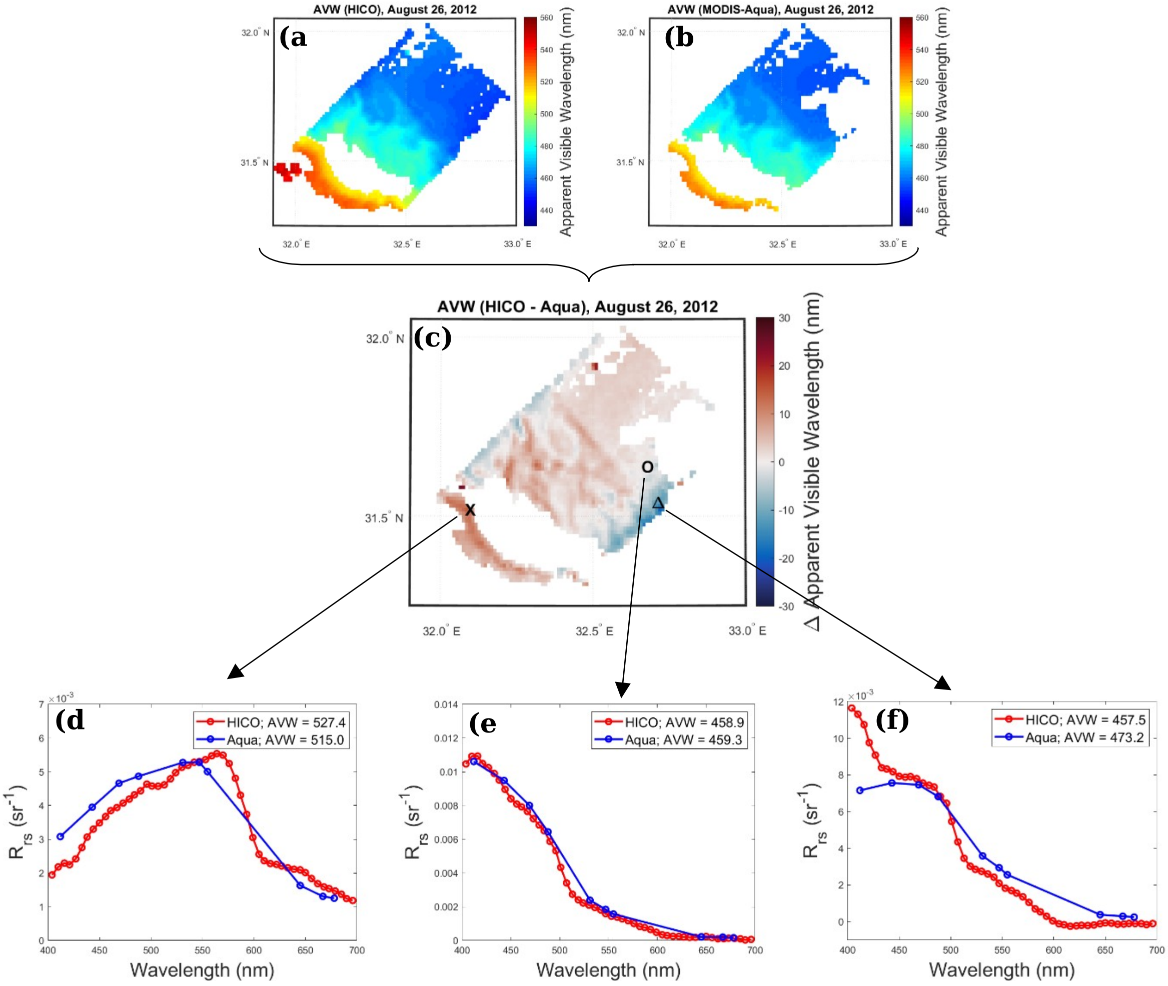

Figure 7. The mapped *AVW* product for (**a**) HICO and (**b**) MODIS-Aqua on August 26, 2012 are qualitatively similar, but a (c) difference image reveals areas where the respective spectra diverge from one another. The image serves as a means to spatially map where HICO spectra are (**d**) red-shifted, (**e**) equivalent, or (**f**) blue-shifted relative to MODIS-Aqua.

3.3. Assessing the fitness-for-purpose of multi-mission trends in AVW

Proceeding with the assurance that *AVW* is a sensitive metric to changes in spectral shape, a careful merging of the satellite record would enable an analysis of 22 years of continuous ocean color trends. However, merging multiple satellite platforms to construct a continuous time-series analysis must be treated with care, as there are spatially and seasonally dependent biases that may be introduced as a result of varying uncertainties between the platforms (Mélin 2016). In order to ensure an added degree of confidence in our ensuing trend analysis, we include a series of diagnostic metrics that assess how much agreement there is between statistics derived from the overlapping time-series of MODIS-Aqua and

SeaWiFS (hereafter denoted as M-S; Jan 2002 – Dec 2007), as well as MODIS-Aqua and VIIRS (hereafter denoted as M-V; Jan 2012 – Dec 2017). Essentially, if there are no glaring discrepancies during periods of overlap coverage, we can be more confident that the merged time-series is not significantly impacted by sensor-specific uncertainties.

The first metric involves constructing a contingency matrix (Sokal and Rohlf 1995), in which we compare the global linear trends (slope of the regression, β) for SeaWiFS and VIIRS relative to the corresponding β for MODIS-Aqua during the respective temporal overlap periods. We separate these trends into three basic categories: non-significant trends (*n.s.,* ($p > 0.05$), significant positive trends ($\beta \geq 0$, $p < 0.05$), or significant negative trends ($\beta \leq 0$, $p < 0.05$) (Table 2). The contingency matrix summarizes the percent of the globe in which all combinations of these three trend diagnostics apply, enabling a simplistic comparison of trend behavior across sensor platforms. The summation of the diagonal elements in the table (where all three diagnostics agree for two sensors) shows that MODIS-Aqua and SeaWiFS are in agreement over 79.3% of the globe, while MODIS-Aqua and VIIRS are in agreement over 82.0% of the globe. The majority of the agreement is in the form of non-significant trends (63.3% for M-S, 60.3% for M-V), which is generally expected, given the short temporal interval of overlap. While the absolute agreement in the directionality of significant trends (16.0% for M-S, 21.7% for M-V) is relatively comparable to the amount of cases in which one sensor detects a significant trend while the other sensor detects a non-significant trend in the same direction (20.7% for M-S, 18.0% for M-V), it is notable that there were no instances in which a significant trend of opposing directionality was detected between two sensors.

Table2. Contingency matrix directly comparing temporal linear trends derived from SeaWiFS and MODIS-Aqua (Jan 2003 – Dec 2007), as well as VIIRS and MODIS-Aqua (Jan 2012 – Dec 2017). The percentage values indicate the percent global coverage in which two diagnostics

%	**SeaWiFS**			**VIIRS**		
MODIS-A	**n.s.**	$\beta \geq 0$	$\beta \leq 0$	**n.s.**	$\beta \geq 0$	$\beta \leq 0$
n.s.	63.3	5.7	3.2	60.3	7.0	2.9
$\beta \geq 0$	8.5	11.0	0	4.8	12.0	0
$\beta \leq 0$	3.3	0	5.0	3.3	0	9.7

The Cohen's κ index can be computed from the values of the contingency matrix, in which we translate the proportional contribution of observed agreement (ρ_o) between two missions relative to the proportion that occurred by chance alone (ρ_c). If we notate the contingency matrix as $(\rho_{i,j})_{i,j} = _{1,n}$ where n = the number of diagnostics (in this case 3, *n.s.,* ($p > 0.05$), ($\beta \geq 0$, $p < 0.05$), and ($\beta \leq 0$, $p < 0.05$), we compute Cohen's κ index as:

$$\kappa = \frac{\rho_o - \rho_c}{1 - \rho_c} \quad (3)$$

where ρ_o represents the summation of the diagonal elements (where both mission trends agree, $\sum_{i=1}^{n} \rho_{i,j}$), while ρ_c represents the sum of the probabilities of chance agreement, $\sum_{i=1}^{n} \left(\sum_{j=1}^{n} \rho_{i,j} \sum_{k=1}^{n} \rho_{k,j} \right)$ (Mélin et al. 2017). The Cohen's κ index indicates moderate agreement between MODIS-Aqua and SeaWiFS (κ = 0.51) and substantial agreement between MODIS-Aqua and VIIRS (κ = 0.62) (Viera and Garrett 2005).

Finally, for each temporally overlapping time-series, the level of significance of a t-test between two pairs yields informs the degree to which trends differ (Mélin et al. 2017). In this case, a significant *p*-value ($p < 0.05$) would indicate that there is a significant difference between the derived trends. For M-S, significant differences were uniformly distributed over 1.7% of the global domain, and for M-V, significant differences were uniformly distributed over 0.9% of the global domain. While there are potential mission-specific artifacts present (Mélin 2016), the results (moderate to substantial agreement between missions, high coherence in trend directionality, and low % significant differences) nonetheless suggest that the constructed 22-year record of *AVW* is fit for analysis of temporal trends, however additional cautionary remarks on interpretation of these trends are further explored in the discussion. Given that our fitness-for-purpose analysis showed that there is substantial agreement between MODIS-Aqua and VIIRS, we opted to use the MODIS-Aqua time series in its entirety rather than switch to VIIRS, since MODIS-Aqua contains twice as much spectral information, and thus is a more sensitive metric of spectral change.

3.4. Examining R_{rs} trends in the spatial and temporal domain

Here, we extend the examination of *AVW* to the 22-year SeaWiFS (1997 -2003) and MODIS-Aqua (2003-2019) time series, as a case study to demonstrate the utility of using *AVW* to emphasize the spatial distribution of linear temporal trends in spectral variability. Essentially, the significant ($p < 0.05$) slope of a robust regression for 22 years of de-trended *AVW* values (monthly time resolution) is plotted for every pixel, enabling the spatial mapping of $\Delta AVW/\Delta year$ over the globe (Figure 8a). The extracted time-series plots of *AVW* (Figures 8e-8g) were generated to highlight the nature of some of these trends (note: a robust evaluation of mechanisms for observed trends exceeds the scope of this analysis). Note, for trend statistics, a continuous time series of data from SeaWiFS (Sep 1997 – Dec 2002) and MODIS-Aqua (Jan 2003 – Dec 2019) were used, while the overlap periods of SeaWiFS (Jan 2003 – Dec 2007) and VIIRS (Jan 2012 – Dec 2020) with MODIS-Aqua are only shown to emphasize spectral continuity across the sensors over time. The slope ($\Delta AVW/\Delta year$) and standard error (*se*) of the robust regression are provided for each extracted area (note, a global plot of *se* as well as *se*/slope can be found in Appendix A). The *se* can be thought of as a measure of the precision with which the regression coefficient is measured (e.g. a low *se*/slope means the trend is not likely zero), and helps determine the relative degree of confidence in a given trend. Figures 8b, 8e demonstrate an illustrative quality control measure, showing the relative spatial-temporal stability of *AVW* values from SeaWiFS/MODIS-Aqua/VIIRS in the oligotrophic Pacific gyre near Hawaii. Other areas display strong negative linear trends such as Lake Michigan (Figures 8c, 8f), while other areas display positive linear trends such as the Patagonian Shelf (Figures 8d, 8g). Note, the substantial agreement in the regionally extracted time-series between VIIRS and MODIS-Aqua (Figures 8e-8g) adds additional confidence to the fitness-for-purpose determination, given that these examples cover stable waters at MOBY, as well as two distinct optically complex environments (one freshwater, one marine). The corresponding time-series of de-trended, spectrally congruent MODIS-Aqua and SeaWiFS R_{rs} channels (λ = 412, 443, 488 (MODIS-Aqua)/ 490 (SeaWiFS), 555, 667 (MODIS-Aqua)/ 670 nm (SeaWiFS); Figures 8h-8j) corroborate the agreement that a diretional (or non-directional) shift in *AVW* equates to a directional (or non-directional) shift in normalized $R_{rs}(\lambda)$, and provides more detail on the nature and evolution of these spectral shifts.

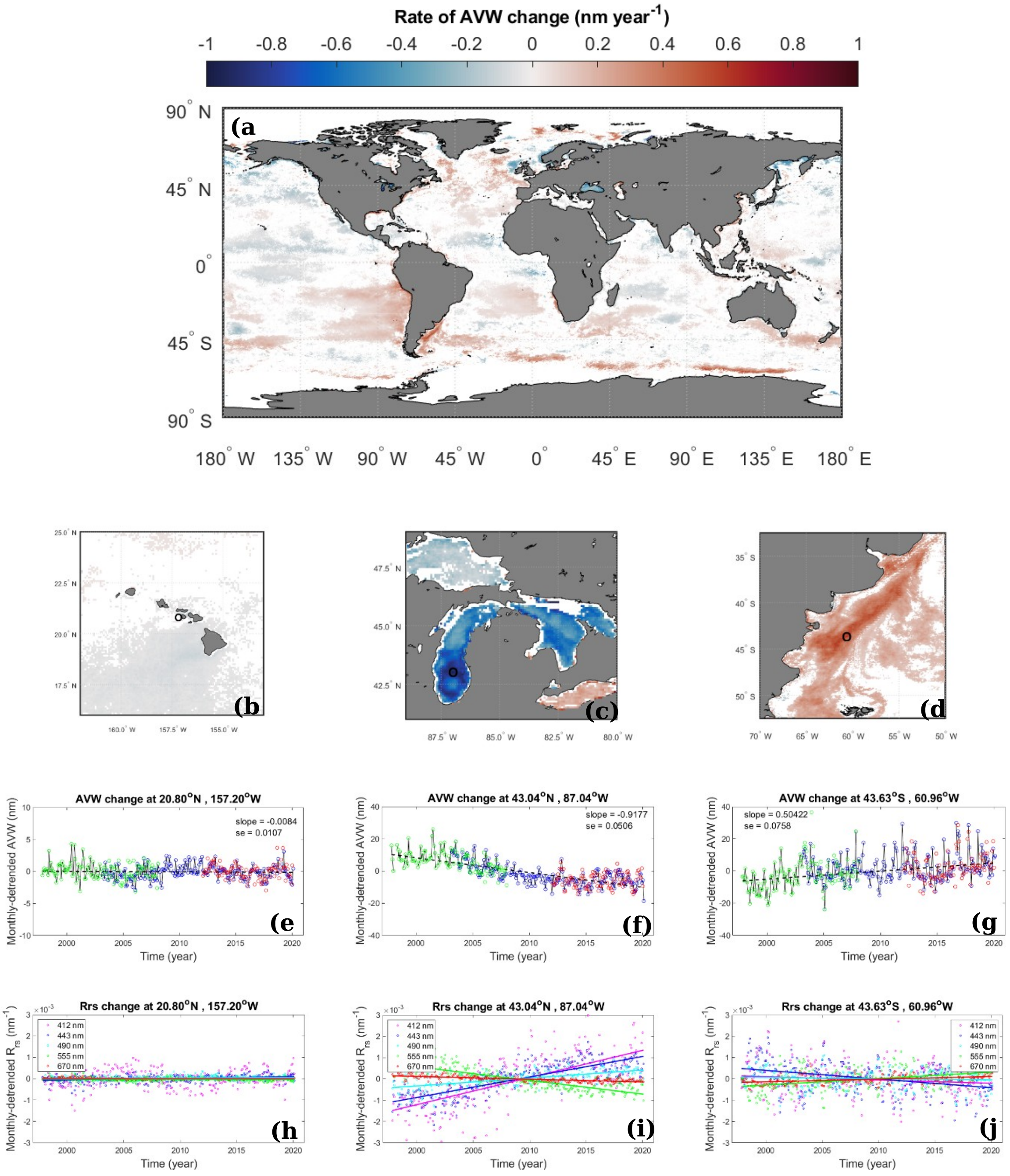

Figure 8. (**a, b, c, d**) Spatial maps of 22-year robust linear trends in *AVW* derived from continuous SeaWiFS (Sep 1997 – Dec 2012) and MODIS-Aqua (Jan 2013 – Dec 2019) data for the globe and extracted subregions, representing a comprehensive spatial-spectral-temporal characterization of all components of ocean color data. A positive slope in the *AVW*/year (i.e. spectral shift towards longer wavelengths) is depicted as red on the map, while a negative slope in the *AVW*/year (i.e. spectral shift towards shorter wavelengths) is depicted as blue on the map. For quality control and demonstrative purposes, extracted time-series of de-trended (monthly) *AVW* (location is marked as a black dot on the subregion maps) are shown for (**e**) the Marine Optical BuoY (MOBY)

site off the coast of Hawaii, (**f**) Lake Michigan, U.S.A., and (**g**) the Patagonian Shelf. The slope and standard error of the regression are displayed on each time-series. The SeaWiFS data (green dots) and VIIRS data (red dots) show similar trends for the overlap period with MODIS-Aqua (blue dots), providing additional quality assurance for cross-sensor comparison. The corresponding time-series of normalized *Rrs(λ)* (**h, i, j**) for each extracted area demonstrates the manifestation of spectral shape change over time (e.g. For Lake Michigan, blue-shifted waters exhibit a steady temporal increase in 410, 443, and 490 nm reflectance, and a decrease in 555 and 670 nm reflectance).

3.5. Examining the spatial-spectral-temporal variability of $R_{rs}(\lambda)$

For enhanced detail in the temporal domain, we can conceptualize simultaneous spectral-spatial-temporal variability of the SeaWiFS (1997-2003) and MODIS-Aqua (2003-2020) time series through the generation of an *AVW* Hovmöller anomaly diagram (Figure 9b) across the North Atlantic 45° parallel (Figure 9a). The anomalies were generated by subtracting *AVW* from the respective monthly climatology (e.g. all *AVW* values in September are subtracted from the average of monthly September values from 1997- 2019). Values are averaged from 44.5° N – 45.5° N and plotted as a function of time across the north Atlantic basin (63.0° W to 1.25° W). The temporal evolution of *AVW* across the North Atlantic shows an apparent increase in *AVW* along the central-western Atlantic from 2014-2018, and an anomalous summer bloom in 2012 representing a red shift in $R_{rs}(\lambda)$ spectra (Figure 9c), and an *AVW* decrease $R_{rs}(\lambda)$ blue-shift in 2005-2006 (Figure 9d).

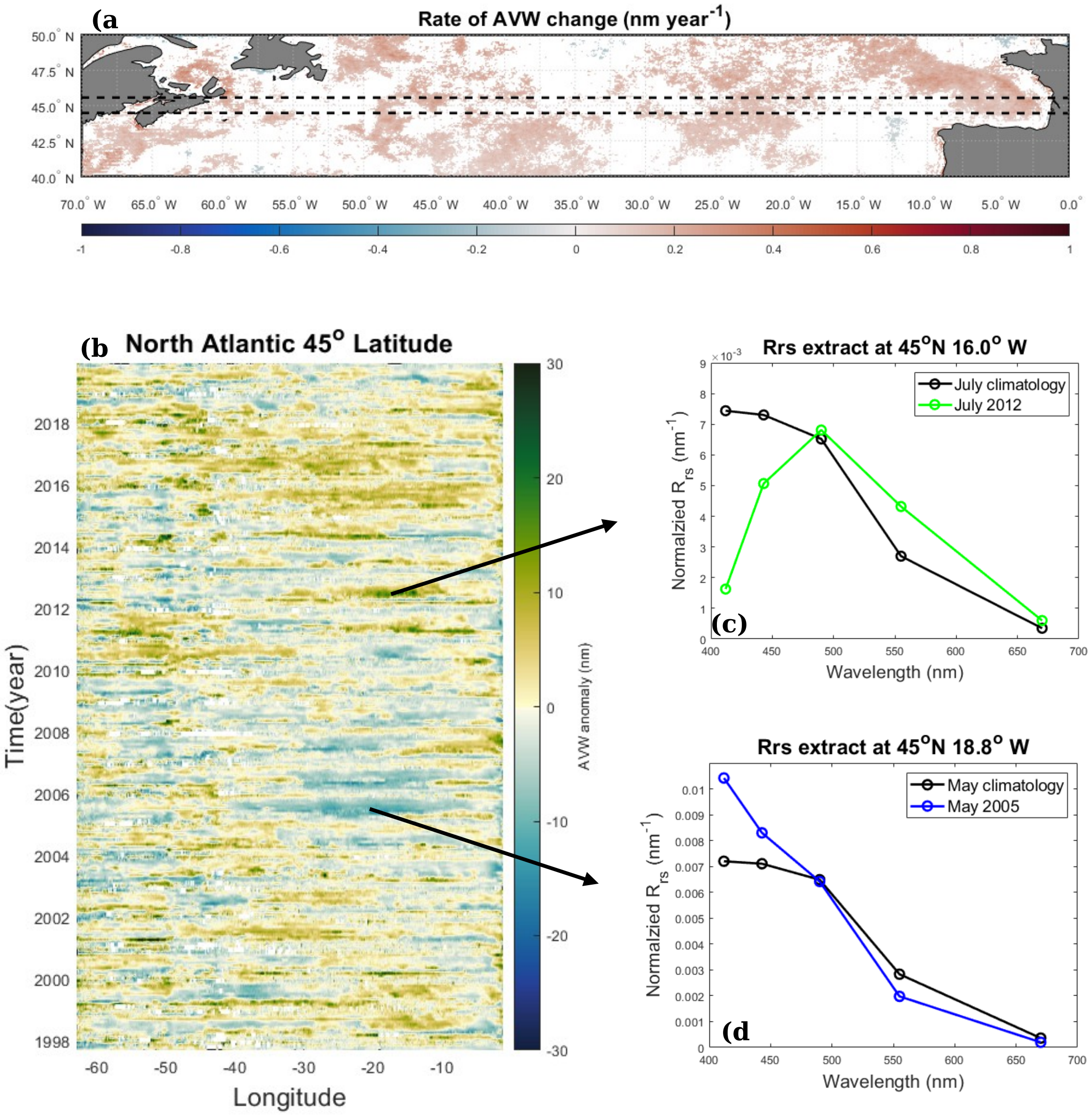
(a
Rate of AVW change (nm year^{-1})
50.0° N
47.5° N
45.0° N
42.5° N
40.0° N
70.0° W
65.0° W
60.0° W
55.0° W
50.0° W
45.0° W
40.0° W
35.0° W
30.0° W
25.0° W
20.0° W
15.0° W
10.0° W
5.0° W
0.0°
-1
-0.8
-0.6
-0.4
-0.2
0
0.2
0.4
0.6
0.8
1
(b
North Atlantic 45° Latitude
Time(year)
2018
2016
2014
2012
2010
2008
2006
2004
2002
2000
1998
-60
-50
-40
-30
-20
-10
Longitude
30
20
10
0
-10
-20
-30
AVW anomaly (nm)
Rrs extract at 45°N 16.0° W
× 10^{-3}
July climatology
July 2012
Normalzied R$_{rs}$ (nm^{-1})
(c)
Wavelength (nm)
400
450
500
550
600
650
700
Rrs extract at 45°N 18.8° W
May climatology
May 2005
Normalzied R$_{rs}$ (nm^{-1})
(d)
Wavelength (nm)

Figure 9. (**a**) Spatial map of 22-year robust linear trends in *AVW* derived from SeaWiFS (1997 – 2003) and MODIS-Aqua (2003 – 2020) over the 45° parallel across the North Atlantic ocean. (**b**) Corresponding Hovmöller anomaly diagram of *AVW* across the 45° parallel. Extracted $R_{rs}(\lambda)$ spectra (congruent MODIS-Aqua/SeaWiFS channels) show the 22-year monthly climatology spectral shape in relation to (**c**) the $R_{rs}(\lambda)$ spectra during an anomalous 2012 summer bloom, as well as (**d**) anomalously blue-shifted waters in May 2005. Dimensional reduction of spatial-spectral-temporal information makes these trends easier to identify.

4. Discussion

4.1. Characteristics of the AVW algorithm

In this manuscript, we present a dynamic technique for simplistic optical water type classification that can be adapted to any spectral dataset to produce a one-dimensional descriptor of spectral shape. The distinct advantage of utilizing *AVW* over discrete spectral classification lies in the derivation of quantitative spectral shape values output along a continuum, providing a transitional gradient with which to analyze trends/differences in optical water types (or sensor output coherence, e.g. Figure 3) across spatial (Figure 7) and temporal (Figure 8) boundaries, or both (Figure 9). Classical clustering methods can carry the burden of relying on an "optimal" definition of output classes, requiring in-depth or a priori knowledge of the dataset to support the initiation of output, and subsequently interpret results. By contrast, the sequence of *AVW* output has meaning in itself (e.g. more red-shifted waters are unequivocally represented by higher numbers, and blue-shifted waters are unequivocally represented by lower numbers), and thus we overcome the limitation of having to minimize/optimize the output to make it more comprehensible. Notably, this negates the absolute necessity to partition the output in order to understand/interpret first-order trends in the data (e.g. is this water parcel more blue/more red?). Though traditional classification schemes are not typically expressed in terms of a gradational or even high frequency output, the *AVW* nevertheless categorically defines (or classifies) $R_{rs}(\lambda)$ according to a shared characteristic (the weighted harmonic mean of $R_{rs}(\lambda)$ wavelengths). By nature of the calculation, the *AVW* exists as an inherent characteristic of the $R_{rs}(\lambda)$, meaning that, unlike many classical clustering methods, the *AVW* of a parcel of water is not dependent on the characteristics of the dataset as a whole. This advantage makes the *AVW* particularly well suited for non-specialists, who may desire a non-subjective classifier which characterizes intuitive spectral information into a simple, quantitative metric. By the same token, it also makes *AVW* well suited to specialists who may endeavor to derive more universal weighting functions for algorithm development based on an optical water type classification that 1) behaves more like a dynamic ocean property, 2) does not need to be trained, and 3) outputs consistent values across multiple datasets.

The concept of using a gradational index for optical water type classification is not novel. Most notably, extensive analyses leading to the development and utilization of the *hue angle* product (van der Woerd and Wernand 2015, 2018; van der Woerd et al. 2016; Wernand et al. 2013) provides many of the same benefits (as well as similar uncertainties) that *AVW* proposes. Though there are some mechanistic differences in the derivation of the two, a global comparison of the two products reveals a very coherent relationship (Figure 10a). On average, each 1-nm increment of *AVW* has a mean absolute deviation of 3.09 *hue angle* degrees. Though the *AVW* algorithm design is less complex in its calculation and does not represent the “true color” as perceived from the human eye, it does offer the unique flexibility to extend the contribution of the UV and NIR into the classification/indexing of spectral signatures. This may be of particular importance in classifying areas with high CDOM contribution, or conversely, high red-edge, NIR contribution (e.g. harmful algae blooms, dense sediment plumes). Additionally, the ability of the *AVW* approach to consider a wider spectral range makes it particularly suitable for analyzing data from NASA's upcoming PACE mission that will extend ocean color measurements to the near UV and NIR/SWIR spectral regions (Werdell et al. 2019). The lack of spectral response sensitivity of the human eye may be the reason for the cubic parabola shape of the relationship between the two products (i.e. higher range of *AVW* values relative to *hue angle* for extreme blue and red-shifted waters), as the 410 nm and 678 nm MODIS channels are minimally weighted by the *hue angle*, but are equally weighted in the *AVW*. Disparities in spectral band detection are also exemplified by the deviations in the relationship between *AVW* and chlorophyll-a (Figure 10b), as the latter is the product of two simultaneous wavelengths, and not the entire spectrum. Even so, close similarities are found between *AVW* and chlorophyll-a in blue-shifted Case-1 ocean waters, where chlorophyll-a (and co-varying CDOM) are the primary drivers of color variability, with increased deviation between the two in red-shifted waters, where there are presumably multiple non-covarying drivers of optical variability.

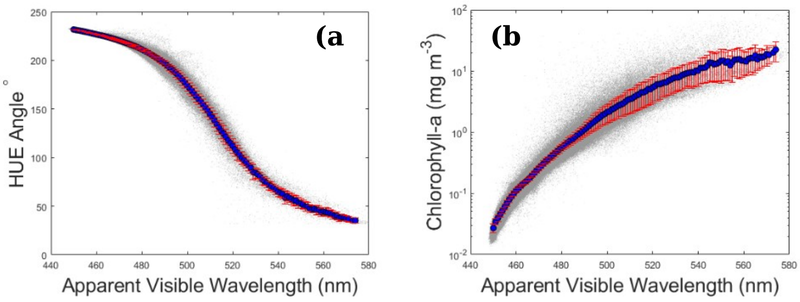

Figure 10. A global comparison of (**a**) *AVW* versus *hue angl*e and (**b**) *AVW* versus *chlorophyll-a* for a MODIS-Aqua 32-day global composite (14 Sep – 15 Oct 2018). The mean (blue dots) and mean absolute deviation (red lines) overlay all global data points (gray dots).

With any optical classification technique, there are limitations and uncertainties associated with spatial and temporal heterogeneity blurring the true optical signal, as well as the multi-spectral resolution of most satellite sensors not capturing the range of optical variability (Mélin and Vantrepotte 2015; Vandermeulen et al. 2017). Hence, while not all water types are explicitly represented in this analysis, the *AVW* may be applied to any variety of datasets with varying temporal/spatial/spectral characteristics. However, it is important to note that this quantitative output is specifically relevant to the spectral shape of reflectance, and does not yield information on the amplitude of reflectance (water brightness). While the absolute variation of $R_{rs}(\lambda)$ amplitude can be highly dependent on the contribution of backscattering components of the water (Lubac and Loisel 2007; Toole and Siegel 2001), by contrast, the spectral shape is more strongly impacted by components contributing to the absorption coefficient, such as phytoplankton, detrital matter, and CDOM (Sathyendranath et al. 1989). As a result, some spectral classes will feasibly contain waters with varying concentrations of particles such as sediments, that lead to the fluctuation in $R_{rs}(\lambda)$ amplitude, but less of a fluctuation in shape (Mélin and Vantrepotte 2015). Thus, assessed independently, the spatial-temporal trends in *AVW* likely have a higher sensitivity to qualitative changes in the types of components contributing to the optical signal, and less the quantity of components, though the two are often closely linked.

We can optionally enhance the use of *AVW* by subdividing the clustered spectra according to the R_{rs} wavelength of maximum reflectance (λ_{MAX}). While not pertinent for algorithm utility, this additional layer of maximum classification can further mitigate variability associated with instances of marginally disparate spectral signatures yielding similar *AVW* numbers (Figure 1, 11a). Similar intra-class spectral shape variance was reported for the *hue angle* product, especially for coastal waters (Lehmann et al. 2018; Pitarch et al. 2019), which is where we find the highest spectral shape uncertainty for global imagery. The uncertainty arises as a result of one portion of the spectral signature yielding a slightly higher/lower weight that is counterbalanced by another portion of the spectral signature, resulting in the same weighted mean. Otherwise stated, more than one spectral shape can result in the same weighted harmonic mean value, therefore anchoring the *AVW* output to λ_{MAX} reduces the amount of spectral deviation for a given *AVW*. In Figure 4b, these disparities are averaged and directly contribute to the level of uncertainty described in Figures 5a and 5b. Figure 11a, on the other hand, represents a duplication of Figure 4b, with the only difference being that the *AVW* output is categorized according to λ_{MAX}., and these disparities in spectral shape within a given *AVW* value are more efficiently partitioned. A histogram (Figure 11b) illustrating the frequency of global *AVW* distribution partitioned by λ_{MAX} demonstrates which *AVW* values are more prone to having overlapping spectral shapes (primarily green waters). Note, in most cases, this overlap has a relatively marginal impact on the bulk spectral shape. This is clearly demonstrated by Figure 1, in which several $R_{rs}(\lambda)$ spectra are characterized by either λ_{MAX}. = 531 nm and λ_{MAX}. = 547 nm, but nonetheless exhibit relative homogeneity in bulk spectral shape.

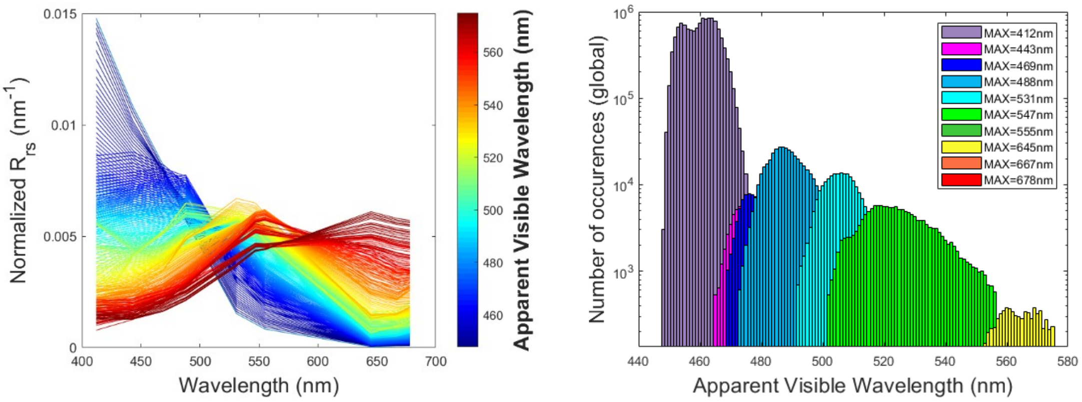

Figure 11. (a) Integral-normalized $R_{rs}\left(\acute{\lambda}\right)_{AVW}$ spectra derived from a 32-day global composite (14 Sep – 15 Oct 2018), with the output additionally portioned according to the wavelength of maximum reflectance (λ_{max}). The addition of maximum classification enables a more effective partitioning of spectral shapes in instances where two or more shapes are represented by the same *AVW*. (b) The global frequency of this may overlap is plotted as a function of *AVW*, revealing areas of spectral ambiguity within the *AVW* index that can be alleviated with maximum classification.

Note, while we found that this subdivision could further reduce the uncertainty for all wavelengths, this also represents another added layer of information, which presents inherent difficulties when conceptualizing or analyzing results in two dimensional space. However, in the case that one or more dimensional constraints can be alleviated (e.g. using *AVW* for algorithm development/deriving weighting functions), the subdivision of *AVW* according to λ_{MAX} can be utilized as a method for further discriminating more subtle differences between spectral shapes. In any case, the utility of *AVW* as a first order index of spectral shifts in areas of higher uncertainty (such as coastal waters) does not hinge on the maximum classification approach. There is, however, an implication that the potential for mis-identification of spectral shapes via the *AVW* approach can lead to potential Type II errors (false negatives, e.g. a spectral shape changes occurs, but is not detected), but not Type I errors (false positives, e.g. a spectral shape change detected when there isn't one), since any change to the *AVW* number represents a true shift in the balance point of the $R_{rs}(\lambda)$ spectrum. Put simply, there are instances in which slightly different spectral shapes may yield the same *AVW* number (and thus a trend would go undetected), but any positive/negative shift in *AVW* will unequivocally represent a respective red/blue directional shift in the spectrum as an inherent function of deriving the weighted harmonic mean. As an additional precautionary measure, the use of an iteratively re-weighted least square regression with a bisquare weighting function adds a layer of assurance that the derivation of temporal trends are less susceptible to influence from acute random error/outliers.

4.2. Spatial-spectral-temporal trends

Reliably defining the full spectrum of $R_{rs}(\lambda)$ in terms of a single number affords the opportunity to examine trends of spectral shape in both the spatial and temporal domain. In term of the spatial domain, the propensity for spectral clustering around a given *AVW* value can be exploited to match spectra of similar shapes, even if they are of disparate spectral resolutions (Figures 3, 7). A promising benefit of the integration of the full spectrum in the *AVW* calculation is having the flexibility to monitor spectral drifts in shorter-term intervals than in-orbit calibrations (e.g. time-series of lunar calibrations), or in the absence of in-orbit calibration altogether (e.g. CubeSat missions). By the very nature of the calculation, any deviations in the spectra are readily manifested as a change in the weighted mean, and thus, *AVW* can serve as a simplistic diagnostic tool to monitor the directionality and magnitude of shifts in the spectral time series in spectrally stable waters, such as at the Marine Optical BuoY (MOBY) or regionally averaged ocean gyres. This has useful implications that would enable cross-sensor comparison of full-spectral performance, which will be imperative in efforts to derive ocean color continuity moving from multi-spectral to hyperspectral satellite monitoring. It is worth noting that spectrally dependent temporal drifts may occur as function of satellite calibration issues or sensor degradation (Meister and Franz 2014), and have the potential to be manifested in the *AVW* signal if not corrected for (Stumpf and Werdell 2010). The performance of vicarious gain adjustment is generally examined one channel at a time, and while hyperspectral radiometry is not exempted, having a means to determine a metric of spectral integrity can be useful to promptly elucidate sensor waveband drift. Without an integrated picture of total $R_{rs}(\lambda)$ variability, it can be challenging to discern optically significant trends using a single wavelength (Jolliff et al. 2018). This underscores the importance of inter-relating multiple dimensions of data, as it is not the absolute reflectance of a single channel (or even the ratio of two channels), but how all channels change relative to one another that determines it unique and intrinsic color, and creates a unique optical water type.

Extending this analysis to a pixel-by-pixel examination of the globe represents a 22-year full spectral-spatial-temporal analysis of ocean color variability from September 1997 to December 2019. While the mechanisms responsible for these spectral shifts extend beyond the scope of this manuscript, some verification of the direction of the derived *AVW* trends remains prudent to provide a quality control check on the performance of the algorithm. On a global scale, many of the temporal shifts in $R_{rs}(\lambda)$ spectral shape (Figure 8a) are related to the spatio-temporal distribution of chlorophyll-a shifts over a similar decadal time frame (Dunstan et al. 2018; Gregg and Rousseaux 2014; Henson et al. 2010; Mélin et al. 2017; Siegel et al. 2013; Vantrepotte and Mélin 2009), which is to be expected given the inherent relationship between chlorophyll-a and water color in Case 1 waters (Figure 10b). As anticipated, no trends are discernable in the MOBY time-series (Figure 8e), providing a useful check on the stability of *AVW* over time in optically stable, oligotrophic waters, as well as a verification of the vicarious calibration of the satellite instruments. The extracted regions corroborate larger shifts documented in the environment over decadal time frames, whether it be an increase in water clarity in Lake Michigan as a function of invasive zebra mussels (Binding et al. 2007) (Figure 8f), or a change in chlorophyll-a concentrations on the Patagonian Shelf due to an increased frequency of shelf break upwelling (Marrari et al. 2017) (Figure 8g).

Interestingly, an early iteration of this analysis, using only 16 years of the MODIS-Aqua time-series, revealed a strong red-shift in ocean color spectra in the eastern North Atlantic (40° – 55° N, 30° - 10° W), corroborated by strong positive temporal trends in the chlorophyll-a record over the same time-frame (Dunstan et al. 2018). While still present in the map we present in this manuscript, the magnitude of this trend was substantially dampened with the addition of only 6 years of SeaWiFS time-series dating back to 1997. Hence, the extracted 45° parallel translated into a Hovmöller diagram enables a closer inference of the temporal evolution in these 22-year spectral trends (Figure 9b). While this diagram shows increasing frequency and duration of red-shifted spectra between 30° W and 10° W occurring more frequently beginning in 2011, and persisting longer in the year, from 2015 – present, the magnitude of this trend was likely artificially amplified by the appearance of anomalous blue-shifted spectra in 2005 and 2006, at least in the context of the MODIS-Aqua time-series. Thus, we impart a strong note of caution in the interpretation of these trends for two reasons: 1) over the time scales observed in this study (22 years of continuous ocean color time series), it is challenging to reconcile long-term trends from that of natural variability including the effect of short-term oceanographic variations (e.g. marine heatwaves) and multi-decadal oscillations (Beaulieu et al. 2013; Cai et al. 2015; Henson et al. 2010; Levitus et al. 2009), and 2) the statistical definition of significance ($p < 0.05$), by which our data are filtered, does not always unequivocally represent a significantly meaningful trend (Bryhn and Dimberg 2011), though we impart some additional quality control by determining the standard error of the regression relative to the magnitude of the trend as a metric of how reliable a trend may be (Figures 8e-8g, Appendix A). For example, the trend in Lake Michigan (Figure 8f) has a *se* representing 5% of the magnitude of the trend, and is considered more reliable than the trend along the Patagonian Shelf (Figure 8g), which exhibits more inter-annual variability and thus a *se* representing 15% of the trend magnitude. This does not contravene the spatial distribution of shifts in the weighted harmonic mean of $R_{rs}(\lambda)$ spectra, but utilizing metrics to examine the reliability of a trend remains a prudent practice. Nevertheless, we emphasize that the intent of the *AVW* is to be used less in terms of a bio-physical parameter, and more as a tool to help elucidate first-order trends in full spectral ocean color data, which always warrant closer examination for each case in order to fully understand the mechanisms responsible for the variation.

5. Conclusion

This study presents a technique to promote the maximum utilization of spectral information for the simultaneous determination of spatial-spectral-temporal trends in ocean color data. We exploit the weighted harmonic mean of $R_{rs}(\lambda)$ wavelengths to yield an intuitive output along a continuum of dominant color values, making the high number of class outputs more manageable and comprehensible when examined in multi-dimensional space. We emphasize the utility of using spectral classification as a useful metric of $R_{rs}(\lambda)$ change along various temporal and spatial scales, and encourage the use of this or other classification techniques for describing any large spectral dataset (e.g. in-line inherent optical properties and hyperspectral radiometry) to unravel spectral variability over large time and space scales. Minimal uncertainty (~5% in blue water, ~10% in green waters) introduced from the algorithm estimation of spectral shape do not appear to impede the analysis of first-order variability in spectral trends, given that the underlying shifts in the spectral weighted mean inherently represent a change in the spectral distribution of $R_{rs}(\lambda)$. At the very least, this technique enables the simple and effective targeting of relative deviations in spectral trends, which, once identified, can be further unraveled with more targeted analysis. With emerging sophistication in passive and active sensor technology, and presumably concomitant increase in data resolution, it is imperative to continue development of techniques to most efficiently conceptualize relationships between multiple dimensions of data.

Author Contributions: **Ryan Vandermeulen**: Conceptualization, Methodology, Writing- Original draft preparation, Software, Formal analysis, Investigation, Visualization, Validation. **Antonio Mannino**: Writing - Review & Editing, Supervision, Resources. **Susanne E. Craig**: Writing - Review & Editing, Data curation. **P. Jeremy Werdell**: Writing - Review & Editing, Project administration.

Funding: This research was funded by the National Aeronautics and Space Administration (NASA) Plankton, Aerosol, Cloud, ocean Ecosystem (PACE) mission.

Acknowledgments: The authors thank the NASA Ocean Biology Processing Group for the processing and distribution of the SeaWiFS/MODIS-Aqua/HICO (https://oceancolor.gsfc.nasa.gov) data. They also thank Jaime Pitarch, Frédéric Mélin, and two anonymous reviewers for invaluable input to this manuscript.

Conflicts of Interest: The authors declare no conflict of interest.

References

Austin, R., & Petzold, T.J. (1981). The determination of the diffuse attenuation coefficient of sea water using the Coastal Zone Color Scanner. *Oceanography from space* (pp. 239-256): Springer

Avouris, D.M., & Ortiz, J. D. (2019). Validation of 2015 Lake Erie MODIS image spectral decomposition using visible derivative spectroscopy and field campaign data. *Journal of Great Lakes Research, 45*, 466-479

Beaulieu, C., Henson, S.A., Sarmiento, J.L., Dunne, J.P., Doney, S.C., Rykaczewski, R., & Bopp, L. (2013). Factors challenging our ability to detect long-term trends in ocean chlorophyll. *Biogeosciences, 10*, 2711-2724

Binding, C.E., Jerome, J.H., Bukata, R.P., & Booty, W.G. (2007). Trends in water clarity of the lower Great Lakes from remotely sensed aquatic color. *Journal of Great Lakes Research, 33*, 828-841

Bryhn, A.C., & Dimberg, P.H. (2011). An operational definition of a statistically meaningful trend. *PLoS One, 6*, e19241

Cai, W., Santoso, A., Wang, G., Yeh, S.-W., An, S.-I., Cobb, K.M., Collins, M., Guilyardi, E., Jin, F.-F., Kug, J.-S., Lengaigne, M., McPhaden, M.J., Takahashi, K., Timmermann, A., Vecchi, G., Watanabe, M., & Wu, L. (2015). ENSO and greenhouse warming. *Nature Climate Change, 5*, 849

CIE, C. (1932). Commission internationale de l'eclairage proceedings, 1931. *Cambridge University, Cambridge*

Craig, S.E., Lee, Z., & Du, K. (2020). Top of Atmosphere, Hyperspectral Synthetic Dataset for PACE (Phytoplankton, Aerosol, and ocean Ecosystem) Ocean Color Algorithm Development. In. PANGEA

Dierssen, H.M., Kudela, R.M., Ryan, J.P., & Zimmerman, R.C. (2006). Red and black tides: Quantitative analysis of water-leaving radiance and perceived color for phytoplankton, colored dissolved organic matter, and suspended sediments. *Limnology and Oceanography, 51*, 2646-2659

Du, K.P., & Lee, Z.P. (2014). Remote-sensing reflectance from above-surface measurements: a revisit based on a coupled ocean-atmosphere mode. In, *Ocean Optics XXII*. Portland, Maine

Dumouchel, W., & O'Brien, F. (1992). Integrating a robust option into a multiple regression computing environment. In, *Computing and graphics in statistics* (pp. 41-48): Springer-Verlag New York, Inc.

Dunstan, P.K., Foster, S.D., King, E., Risbey, J., O’Kane, T.J., Monselesan, D., Hobday, A.J., Hartog, J.R., & Thompson, P.A. (2018). Global patterns of change and variation in sea surface temperature and chlorophyll a. *Scientific reports, 8*, 14624

Eleveld, M., Ruescas, A., Hommersom, A., Moore, T., Peters, S., & Brockmann, C. (2017). An optical classification tool for global lake waters. *Remote Sensing, 9*, 420

Gregg, W.W., & Rousseaux, C.S. (2014). Decadal trends in global pelagic ocean chlorophyll: A new assessment integrating multiple satellites, in situ data, and models. *Journal of Geophysical Research: Oceans, 119*, 5921-5933

Henson, S.A., Sarmiento, J.L., Dunne, J.P., Bopp, L., Lima, I.D., Doney, S.C., John, J.G., & Beaulieu, C. (2010). Detection of anthropogenic climate change in satellite records of ocean chlorophyll and productivity. *Biogeosciences, 7*, 621–640

Hestir, E.L., Brando, V.E., Bresciani, M., Giardino, C., Matta, E., Villa, P., & Dekker, A.G. (2015). Measuring freshwater aquatic ecosystems: The need for a hyperspectral global mapping satellite mission. *Remote Sensing of Environment, 167*, 181-195

Holland, P.W., & Welsch, R.E. (1977). Robust regression using iteratively reweighted least-squares. *J Communications in Statistics-theory and methods, 6*, 813-827

Ibrahim, A., Franz, B., Ahmad, Z., Healy, R., Knobelspiesse, K., Gao, B.-C., Proctor, C., & Zhai, P.-W. (2018). Atmospheric correction for hyperspectral ocean color retrieval with application to the Hyperspectral Imager for the Coastal Ocean (HICO). *Remote Sensing of Environment, 204*, 60-75

IOCCG (2006). Remote sensing of inherent optical properties: fundamentals, tests of algorithms, and applications. In Z. Lee (Ed.), *Reports of the International Ocean-Colour Coordinating Group*

ISO, I., & OIML, B. (1995). Guide to the Expression of Uncertainty in Measurement. *Geneva, Switzerland, 122*

Jolliff, J.K., Jarosz, E., Ladner, S., Smith, T., Anderson, S., & Dykes, J. (2018). The Optical Signature of a Bottom Boundary Layer Ventilation Event in the Northern Gulf of Mexico's Hypoxic Zone. *J Geophysical Research Letters, 45*, 8390-8398

Kirk, J.T. (1994). *Light and photosynthesis in aquatic ecosystems*. Cambridge university press

Lee, S., Meister, G., & Franz, B. (2019). MODIS Aqua Reflective Solar Band Calibration for NASA’s R2018 Ocean Color Products. *Remote Sensing, 11*, 2187

Lehmann, M., Nguyen, U., Allan, M., & van der Woerd, H. (2018). Colour classification of 1486 lakes across a wide range of optical water types. *Remote Sensing, 10*, 1273

Levitus, S., Matishov, G., Seidov, D., & Smolyar, I. (2009). Barents Sea multidecadal variability. *Geophysical Research Letters, 36*

Lubac, B., & Loisel, H. (2007). Variability and classification of remote sensing reflectance spectra in the eastern English Channel and southern North Sea. *Remote Sensing of Environment, 110*, 45-58

Maritorena, S., Siegel, D.A., & Peterson, A.R. (2002). Optimization of a semianalytical ocean color model for global-scale applications. *Applied optics, 41*, 2705-2714

Marrari, M., Piola, A.R., & Valla, D. (2017). Variability and 20-year trends in satellite-derived surface chlorophyll concentrations in large marine ecosystems around South and Western Central America. *Frontiers in Marine Science, 4*, 372

Meister, G., & Franz, B.A. (2014). Corrections to the MODIS aqua calibration derived from MODIS aqua ocean color products. *IEEE Transactions on Geoscience and Remote Sensing, 52*, 6534-6541

Mélin, F. (2016). Impact of inter-mission differences and drifts on chlorophyll-a trend estimates. *International Journal of Remote Sensing, 37*, 2233-2251

Mélin, F., & Vantrepotte, V. (2015). How optically diverse is the coastal ocean? *Remote Sensing of Environment, 160*, 235-251

Mélin, F., Vantrepotte, V., Chuprin, A., Grant, M., Jackson, T., & Sathyendranath, S. (2017). Assessing the fitness-for-purpose of satellite multi-mission ocean color climate data records: A protocol applied to OC-CCI chlorophyll-a data. *Remote Sensing of Environment, 203*, 139-151

Mobley, C.D., & Sundman, L.K. (2008). HYDROLIGHT 5 ECOLIGHT 5. *Sequoia Scientific Inc*

Moore, T.S., Campbell, J.W., & Dowell, M.D. (2009). A class-based approach to characterizing and mapping the uncertainty of the MODIS ocean chlorophyll product. *Remote Sensing of Environment, 113*, 2424-2430

Moore, T.S., Dowell, M.D., Bradt, S., & Verdu, A.R. (2014). An optical water type framework for selecting and blending retrievals from bio-optical algorithms in lakes and coastal waters. *Remote Sensing of Environment, 143*, 97-111

O'Reilly, J.E., & Werdell, P.J. (2019). Chlorophyll algorithms for ocean color sensors-OC4, OC5 & OC6. *Remote Sensing of Environment, 229*, 32-47

Pitarch, J., van der Woerd, H.J., Brewin, R.J., & Zielinski, O. (2019). Optical properties of Forel-Ule water types deduced from 15 years of global satellite ocean color observations. *Remote Sensing of Environment, 231*, 111249

Prasad, D., & Agarwal, K. (2016). Classification of hyperspectral or trichromatic measurements of ocean color data into spectral classes. *Sensors, 16*, 413

Ricchiazzi, P., Yang, S., Gautier, C., & Sowle, D. (1998). SBDART: A research and teaching software tool for plane-parallel radiative transfer in the Earth's atmosphere. *Bulletin of the American Meteorological Society, 79*, 2101-2114

Sathyendranath, S., Prieur, L., & Morel, A. (1989). A three-component model of ocean colour and its application to remote sensing of phytoplankton pigments in coastal waters. *International Journal of Remote Sensing, 10*, 1373-1394

Schaepman, M.E., Ustin, S.L., Plaza, A.J., Painter, T.H., Verrelst, J., & Liang, S. (2009). Earth system science related imaging spectroscopy—An assessment. *Remote Sensing of Environment, 113*, S123-S137

Siegel, D.A., Behrenfeld, M.J., Maritorena, S., McClain, C.R., Antoine, D., Bailey, S.W., Bontempi, P.S., Boss, E.S., Dierssen, H.M., & Doney, S.C. (2013). Regional to global assessments of phytoplankton dynamics from the SeaWiFS mission. *Remote Sensing of Environment, 135*, 77-91

Sokal, R., & Rohlf, F. (1995). Biometry: the principles and practice of statistics in biological research. *WH Freeman, New YorkTejerina-Garro FL, Fortin R, Rodriguez MA (1998) Fish community structure in relation to environmental variation in floodplain lakes of the Araguaia River, Amazon Basin. Environ Biol Fishes, 51*, 399410Valrio

Stumpf, R.P., & Werdell, P.J. (2010). Adjustment of ocean color sensor calibration through multi-band statistics. *Optics express, 18*, 401-412

Toole, D.A., & Siegel, D.A. (2001). Modes and mechanisms of ocean color variability in the Santa Barbara Channel. *Journal of Geophysical Research: Oceans, 106*, 26985-27000

Ule, W. (1892). Die bestimmung der Wasserfarbe in den Seen. *Kleinere Mittheilungen. Dr. A. Petermanns Mittheilungen aus Justus Perthes geographischer Anstalt*, 70-71

van der Woerd, H., & Wernand, M. (2015). True colour classification of natural waters with medium-spectral resolution satellites: SeaWiFS, MODIS, MERIS and OLCI. *Sensors, 15*, 25663-25680 van der Woerd, H., & Wernand, M. (2018). Hue-angle product for low to medium spatial resolution optical satellite sensors. *Remote Sensing, 10*, 180

van der Woerd, H.J., Wernand, M., Peters, M., Bala, M., & Brochmann, C. (2016). True color analysis of natural waters with SeaWiFS, MODIS, MERIS and OLCI by SNAP. *Proceedings of the Ocean Optics XXIII, Victoria, BC, Canada*, 23-28

Vandermeulen, R.A., Mannino, A., Neeley, A., Werdell, J., & Arnone, R. (2017). Determining the optimal spectral sampling frequency and uncertainty thresholds for hyperspectral remote sensing of ocean color. *Optics express, 25*, A785-A797

Vantrepotte, V., Loisel, H., Dessailly, D., & Mériaux, X. (2012). Optical classification of contrasted coastal waters. *Remote Sensing of Environment, 123*, 306-323

Vantrepotte, V., & Mélin, F. (2009). Temporal variability of 10-year global SeaWiFS time-series of phytoplankton chlorophyll a concentration. *ICES Journal of Marine Science, 66*, 1547-1556

Viera, A.J., & Garrett, J.M. (2005). Understanding interobserver agreement: the kappa statistic. *Fam med, 37*, 360-363

Wei, J., Lee, Z., & Shang, S. (2016). A system to measure the data quality of spectral remote-sensing reflectance of aquatic environments. *Journal of Geophysical Research: Oceans, 121*, 8189-8207

Werdell, P.J., Behrenfeld, M.J., Bontempi, P.S., Boss, E., Cairns, B., Davis, G.T., Franz, B.A., Gliese, U.B., Gorman, E.T., & Hasekamp, O. (2019). The Plankton, Aerosol, Cloud, ocean Ecosystem (PACE) mission: Status, science, advances. *Bulletin of the American Meteorological Society*

Wernand, M., Hommersom, A., & van der Woerd, H.J. (2013). MERIS-based ocean colour classification with the discrete Forel-Ule scale. *Ocean Science, 9*, 477-487

Ye, H., Li, J., Li, T., Shen, Q., Zhu, J., Wang, X., Zhang, F., Zhang, J., & Zhang, B. (2016). Spectral classification of the Yellow Sea and implications for coastal ocean color remote sensing. *Remote Sensing, 8*, 321